






Direct imaging of photonic band-edge states in golden Vogel spirals using photoemission electron microscopy

MARTIN AESCHLIMANN,¹ TOBIAS BRIXNER,²  FELIX FENNER,³ BENJAMIN FRISCH,¹ PATRICK FOLGE,^{3,4} MICHAEL HARTELT,¹ MATTHIAS HENSEN,² THOMAS H. LOEBER,⁵ WALTER PFEIFFER,^{3,*}  SEBASTIAN PRES,²  AND BERND STANNOWSKI⁶

¹Fachbereich Physik and Research Center OPTIMAS, TU Kaiserslautern, Erwin-Schrödinger-Str. 46, 67663 Kaiserslautern, Germany

²Institut für Physikalische und Theoretische Chemie, Universität Würzburg, Am Hubland, 97074 Würzburg, Germany

³Fakultät für Physik, Universität Bielefeld, Universitätsstr. 25, 33615 Bielefeld, Germany

⁴Current address: Department Physik - Angewandte Physik, Universität Paderborn, Warburger Straße 100, 33098 Paderborn, Germany

⁵Nano-Structuring-Center, Erwin-Schrödinger-Str. 13, 67663 Kaiserslautern, Germany

⁶Helmholtz-Zentrum Berlin für Materialien und Energie GmbH, Schwarzschildstr. 3, 12489 Berlin, Germany

*Corresponding author: pfeiffer@physik.uni-bielefeld.de

Received 2 November 2022; revised 8 January 2023; accepted 10 January 2023; posted 10 January 2023; published 9 February 2023

Golden Vogel spirals, as deterministic aperiodic structures, support isotropic photonic band gaps and have interesting applications. Localized modes, such as band-edge states, are essential for tailored light–matter interaction. Here we report imaging of such modes using photoemission electron microscopy (PEEM). Tunable ultrashort light pulses excite them in golden Vogel spirals that were fabricated by focused-ion-beam (FIB) milling of an a-Si:H layer. The local near-field leads to electron emission, which is detected spatially resolved. The demonstration of FIB-textured a-Si:H as photonic material and the ability of mode imaging by PEEM offers means to spatiotemporally resolve mode dynamics and to perform nanospectroscopy. © 2023 Optica Publishing Group

<https://doi.org/10.1364/JOSAB.479667>

1. INTRODUCTION

Spiral lattices provide an interesting platform for generating deterministic structures that lack translational and orientational symmetries [1]. In particular, Vogel spirals [2] have found wide recognition in disordered photonics since a simple design rule allows constructing aperiodic optical media [3–5]. For aperiodic Vogel arrays, quite a few interesting photonic properties were reported. The aperiodic structure of so-called golden Vogel spirals is based on an irrational angle that determines the placement of the subsequent element of the spiral structure. Because of this, its Fourier transform, and thus also interesting properties such as the photonic band gap, are isotropic [1,6,7]. This is a significant advantage over other deterministic photonic structures, such as quasicrystals, which are anisotropic. Dal Negro and coworkers have identified localized band-edge states and orbital angular-momentum states of light in these golden spiral structures [7,8]. In particular, the localized states are interesting because they offer the possibility to enhance light–matter interaction for dye molecules or quantum dots that are brought into the vicinity of the spiral. Based on this concept, broadband light scattering and luminescence enhancement were realized [8–10]. Cavity quality factors of more than 2000 were demonstrated for these localized modes in Si₃N₄-based Vogel spirals [5,11]. These are just some

selected examples of the fascinating photonic properties of these structures, which start to be implemented in metasurfaces and more complex optical antenna designs [12].

For all future applications of Vogel spirals in photonic devices, detailed knowledge of the local field inside the structure is essential. To the best of our knowledge, there are only two experiments reported in the literature that directly probe the fields within a 2D spiral structure. One relies on the off-resonant excitation of Er centers in Er-doped dielectric pillars and locally resonance-enhanced photoluminescence (PL) emission [8] and thus is sensitive only for modes that have spectral overlap with the Er–PL related transition. The other employs scanning near-field optical microscopy (SNOM) [13]. In this case SNOM images were stitched together to reveal local fields in a 50- μ m-diameter Vogel spiral ($\alpha = 137.3^\circ$, i.e., a nearly golden spiral) for illumination at the telecommunication wavelength of 1556 nm. Only very recently, both luminescence enhancement microscopy [9,10] and cavity-enhanced light–matter interaction in spirals [5,11] provided additional, however rather indirect, probes for the field distribution within the spiral structure.

Here we overcome this limitation and exploit femtosecond laser-induced photoemission electron microscopy (PEEM) to map local field distributions within a Vogel spiral without

the need for time-consuming lateral scanning. In the applied technique, optical fields inside the material excite electrons in a nonlinear process to states above the vacuum energy, which then might be emitted and detected with spatial resolution using PEEM. Over almost two decades this method has proven to be highly valuable for the characterization, control, and spectroscopy of plasmon–polariton excitations [14–17]. However, the method is not restricted to metals; also, dielectrics can be studied if their conductivity is sufficiently high to avoid surface charging effects. For example, amorphous Si layers, as they are used in photovoltaics or thin-film transistors, also provide a suitable substrate for investigating photonic effects [18].

2. SAMPLE DESIGN AND FABRICATION

The sample design is based on hydrogenated amorphous silicon (a-Si:H) layers as they are employed in thin-film photovoltaics. In the investigated wavelength regime between 750 and 900 nm, a-Si:H is only weakly absorbing, with an absorption length larger than $10\ \mu\text{m}$ [19]. This makes this material well suited to study the absorption enhancing effect of nanotexturing the absorber films. In commercial a-Si:H photovoltaic cells, nanotextured transparent conductive oxide (TCO) layers are used and the deposition of an a-Si:H layer forms a nanotextured layer with almost the same surface texture as that of the TCO substrate. In such films, light is efficiently scattered and the efficiency of photovoltaic cells employing such nanotextured layers is significantly enhanced [7]. In a previous PEEM-based study, we demonstrated Anderson localization and perfect absorption for such nanostructured layers revealing a very short mean free path of about 60 nm for the waveguide modes in the layer [18]. Such a-Si:H layers form an ideal platform for investigating light trapping in disordered structures because they combine a rather weak absorption at sufficiently long wavelength and many possibilities to tailor the absorber layer geometry.

Here we chose a completely different approach for nanotexturing the a-Si:H layer, i.e., perforating the absorber layer by

nanoholes, which can be deterministically fabricated using focused-ion-beam (FIB) methods. Nanohole-textured disordered 2D waveguides are well known to enable, for example, Anderson localization [20], and they allow for advanced photon management [21]. Adopting this concept, a rather smooth a-Si:H layer [root-mean-square (rms) roughness of $\sim 4\ \text{nm}$] on top of a TCO layer serves as photonic waveguide, and the thickness is chosen to support the fundamental modes for excitation around 800 nm. The FIB milled holes in this waveguide then scatter light propagating in the waveguide. Based on this design concept, finite-difference time-domain (FDTD) simulations were used to optimize both the waveguide behavior of the a-Si:H layer for 800 nm light and the nanohole diameter (Fig. 1). The commercial FDTD solver in the CST STUDIO SUITE was employed here to determine the scattering efficiency of individual holes in such a waveguide structure. The total calculation area is $1\ \mu\text{m} \times 5\ \mu\text{m}$, the structure was discretized with grid resolution of 10 nm, and the results were checked for convergence of the obtained results upon changing the grid resolution.

For 150 nm thickness of the a-Si:H layer, the light is efficiently guided in the layer primarily as TM $m=0$ and TE $m=1$ modes. However, in the highly disordered structures investigated here, these waveguide modes are no longer dominating, but strong scattering of the waves leads to mode mixing. As expected, the 2D scattering cross section σ_{2D} of the nanohole (not shown) increases with the hole radius. From the absolute value and the nanohole fill factor f , which is defined as the ratio between the total hole area and the sample surface, the mean free path l_{mfp} of a waveguide mode in a random nanohole distribution with non-overlapping holes is estimated using $l_{\text{mfp}} = (f2\pi R^2\sigma_{2D})^{-1}$ and shown in Fig. 1(c). Already at $f=0.3$, l_{mfp} does not get smaller and saturates at $l_{\text{mfp}} \sim 500\ \text{nm}$ with increasing fill factor, indicating the very efficient scattering by the nanoholes. The minimum mean free path is reached for a hole radius of about 65 nm. For smaller holes, the scattering efficiency of an individual hole becomes too small and thus l_{mfp} increases even for large fill factors. For larger

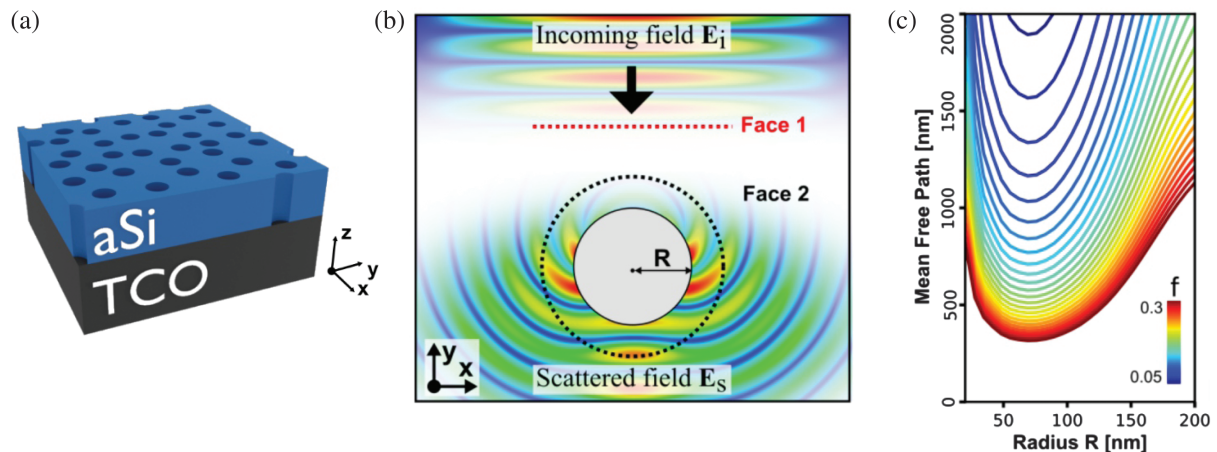


Fig. 1. Nanohole optimization for efficient in-plane scattering of waveguide modes in the 2D a-Si:H layer. (a) Schematic of the layer structure. On top of a smooth 400-nm-thick TCO layer on glass, a 150-nm-thick a-Si:H layer is deposited, and subsequently nanoholes are milled using FIB. (b) Schematic of FDTD simulations (CST STUDIO SUITE) used to optimize the hole diameter for efficient scattering at 800 nm. The scattering cross section is determined for a single air-filled nanohole in the film by calculating the ratio of the incoming energy flux (face 1) and the scattered power (face 2). Purely real refractive indices $n_{\text{a-Si:H}} = 3.9$ and $n_{\text{TCO}} = 1.6$ are assumed for a-Si:H and TCO, respectively. (c) Mean free path l_{mfp} for air-filled nanoholes in a-Si:H waveguide as function of nanohole radius R and fill factor f .

hole radii, the mean separation of the holes increases and thus l_{mfp} increases as well.

For sample preparation, the amorphous Si layers were deposited by means of plasma-enhanced chemical vapor deposition (PECVD) on TCO-coated glass. In this process, a-Si:H films were deposited on the substrate at temperatures between 200 and 250°C. As a substrate, we employed aluminum-doped zinc oxide (ZnO:Al) in the form of a TCO layer on glass. This was direct current (DC) magnetron-sputtered at substrate temperatures in the range of 300°C, which resulted in a smooth ZnO:Al surface topology with a rms roughness of ~ 4 nm.

The two different Vogel spiral patterns investigated here are shown in Fig. 2. The set of hole positions $\{r_i, \vartheta_i\}$ in polar coordinates was generated by $r_i = a\sqrt{i}$ and $\vartheta_i = i\alpha$, with $i \in \{0, 1, 2, \dots, n_{\text{max}}\}$ and the two parameters a , as scaling factor, and α , the divergence angle. Here, the irrational golden angle $\alpha = 1440/(1 + \sqrt{5})^2 \approx 137.508^\circ$ was used to create both golden spirals $f_{0.1}$ and $f_{0.2}$, where the f reminds of the filling factor, which differs between both spirals. It yields the depicted uniform spirals because it is based on an irrational ratio of subsequent Fibonacci numbers. As seen in 2D Fourier transforms, these golden spiral structures exhibit no orientational or translational symmetries [3]. Already a small deviation in the angle of, e.g., 0.1° alters the shape of the spiral towards separating arms with increasing radius.

The Vogel spiral pattern of holes was created by FIB milling. To achieve holes with the desired radius of 65 nm, each hole was parameterized as a ring-shaped groove of 60 nm radius. This, in combination with the FIB cutting profile, led to holes with 130 nm diameter. Note that the FIB cut in the a-Si:H layer has somewhat tilted slopes and thus the holes are not perfectly cylindrical. At the upper side of the a-Si:H layer, the hole radius is about 20 nm larger than at the lower side. Since the waveguide mode interacts with the whole hole, these deviations from an ideal cylindrical structure are averaged out and do not significantly reduce the scattering efficiency.

3. METHODS

The optical excitation of the Vogel spirals was investigated by PEEM. Ultrashort light pulses, incident close to the surface normal (with an incidence angle $\approx 4^\circ$), were coupled into the a-Si:H layer via scattering at the nanoholes. The electromagnetic field distribution in the absorber layer led to electronic excitation and in turn to both multiphoton electron emission and thermionic emission of electrons [18]. The lateral electron emission pattern was detected using ultra-high-vacuum (UHV) PEEM with a nominal spatial resolution of ~ 40 nm. Based on this detection scheme, the method is sensitive to the local enhancement of electromagnetic energy within the absorber layer and can thus resolve optical near-field distributions and non-radiative modes. In the presented experiments, the PEEM was operated using a charge-coupled-device (CCD) camera for emission pattern detection.

As a femtosecond laser, we used a Ti:sapphire oscillator (MaiTai HP oscillator, Spectra Physics) that provided remotely tunable ultrashort laser pulses over a wavelength range from 690 to 1040 nm with a repetition rate of 80 MHz and a pulse length below 100 fs. To correct for variations of the pulse energy over this tuning range and the non-constant response of optical components, the laser power entering the UHV chamber was actively stabilized. Thus, we achieved a constant peak laser intensity corresponding to an average power of about 1 W on the sample over the whole tuning range. The laser pulses were weakly focused onto the sample using a lens positioned outside the UHV chamber. An illuminating spot size of ~ 50 μm diameter was achieved on the sample. Hence, across the investigated Vogel spirals with total diameters of 20 μm , a rather homogeneous illumination is guaranteed.

FDTD simulation of the full 3D $f_{0.2}$ spiral structure were performed using the ANSYS Lumerical Software ULC (Finite Difference IDE R2.5 2021, Version 8.26.2885) for near normal incidence illumination (incidence angle 4°) with p -polarized light. The 150-nm-thick a-Si:H layer was meshed with a resolution of 10 nm in the lateral direction and 15 nm in the vertical

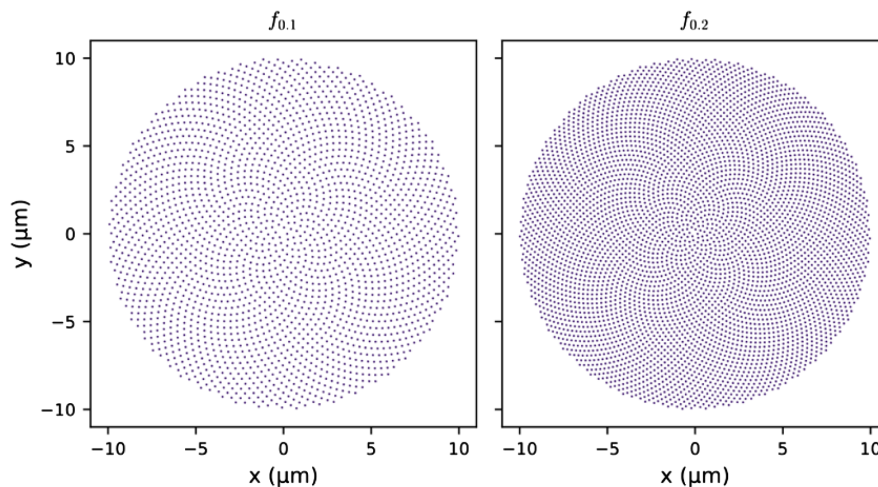


Fig. 2. Geometry of two Vogel spiral structures labeled $f_{0.1}$ and $f_{0.2}$. Each dot represents a 130-nm hole in the a-Si:H-layer. The left and right panels show structures with fill factors $f = 0.1$ (2367 holes) and $f = 0.2$ (4734 holes), respectively. In both cases the golden angle $\alpha \approx 137.508^\circ$ is chosen. $a = 0.2$ and $a = 0.145$ (Vogel spiral scaling factor as defined in main text) generate the pattern with low and high fill factor, respectively. Note that here only the centers of the hole positions and not the shapes of the holes themselves are indicated.

direction. Outside this region, the mesh size is increased to a minimum number of 20 points per wavelength in the vertical direction, depending on the refractive index of the material of interest. Here we have used the complex-valued refractive index data of Pierce and Spicer [22] for the a-Si:H substrate, and that of König and co-workers for the ITO substrate [23].

4. RESULTS AND DISCUSSION

The electron emission patterns from the two Vogel spirals recorded with PEEM are shown in Fig. 3 for different excitation wavelengths. A maximum yield of about 5×10^3 counts per second (cps) was observed for an unusually high pump power around 1 W, when compared to the typically one order of magnitude lower laser power needed for such yields from nanostructured metallic samples. The counts in Fig. 3 correspond to the uncalibrated CCD output. However, the CCD gain was unchanged throughout all measurements, and thus the obtained yields can be directly compared. As mentioned above, in comparison to plasmonic nanostructures, the emission yield is rather low. This is attributed to the fact that absorption in the a-Si:H layer is rather weak. Thus, the electromagnetic field induced within the a-Si:H waveguide layer under normal illumination neither leads to efficient direct multiphoton electron emission nor does it locally heat the electronic system sufficiently to support thermionic emission. Notably, around 850 nm the yield is significantly enhanced. This qualitatively agrees well with the design concept. The nanoholes were optimized to yield the shortest possible mean free path l_{mfp} for light propagating in the waveguide layer and thus also scatter efficiently around 800 nm [see Figs. 1(b) and 1(c)]. Accordingly, the excitation of modes in this wavelength range should be favored.

In addition to the general emission enhancement, a clear mode structure that changes with the excitation wavelength is apparent. In all emission patterns, clear ring structures appear. The structure and size of these rings vary significantly with wavelength. Either “closed rings,” as best seen in the patterns recorded at 750 nm, or “dipolar lobes,” as best seen for $f_{0.2}$ at 850 nm excitation, appear. Although an enhanced electron emission yield indicates a stronger excitation and thus enhanced local light fields within the a-Si:H waveguide layer,

this observation does not directly reveal the reason for this enhancement. A particular local structure of the spiral pattern, i.e., an arrangement of the nanoholes that provides the wave vector components required to couple the incident wavelength into the waveguide, might, for example, favor the coupling between incident light and the layer and thus give rise to stronger local fields and excitation inside the layer. Alternatively, the coupling into the waveguide might be rather homogeneous, and the light scattered into the waveguide is then trapped in photonic modes supported by the spiral structure. Hence the rings seen in Fig. 3 reveal either a variation of the coupling into the waveguide or photonic modes in the golden Vogel spiral or both.

The mode patterns differ between the two spirals for a given excitation wavelength. This is best seen for the “dipolar lobe” pattern at 850 nm in the $f_{0.2}$ spiral, which appears only at 900 nm excitation in the $f_{0.1}$ spiral. In addition, the “closed circle” pattern is observed at 800 nm in $f_{0.2}$ and at 850 nm in $f_{0.1}$. Hence, in the more loosely packed Vogel spiral the mode patterns appear shifted towards ~ 50 nm higher wavelengths compared to the more densely packed spiral. Note that for the more tightly packed spiral ($f_{0.2}$) the emission pattern exhibits less granularity and varies rather smoothly so that the underlying hole pattern is only slightly visible. In contrast, the more loosely packed spiral $f_{0.1}$ exhibits a more granular emission pattern. This is attributed to the lower fill factor, which leads to less efficient coupling to the spiral structure and thus more pronounced emission from individual nanoholes. Such emission from individual holes arises from shape edges and local irregularities and does not reflect the excitation of the a-Si:H layer. Because of the lower granularity of the emission pattern for spiral $f_{0.2}$ the spatial pattern of the excitation in the a-Si:H layer is much more visible. Since the main objective of the present investigation is the identification of localized band-edge states in the photonic spiral structure, we focus in the following on the more tightly packed Vogel spiral $f_{0.2}$.

The changing emission pattern as a function of the excitation wavelength in the range between 750 and 900 nm is shown for the Vogel $f_{0.2}$ spiral in Fig. 4 with more intermediate wavelength steps than in Fig. 3. Up to 800 nm, mostly three closed ring modes appear. From 840 up to 870 nm, a dipolar lobe pattern forms in three rings. The lobes are oriented along the

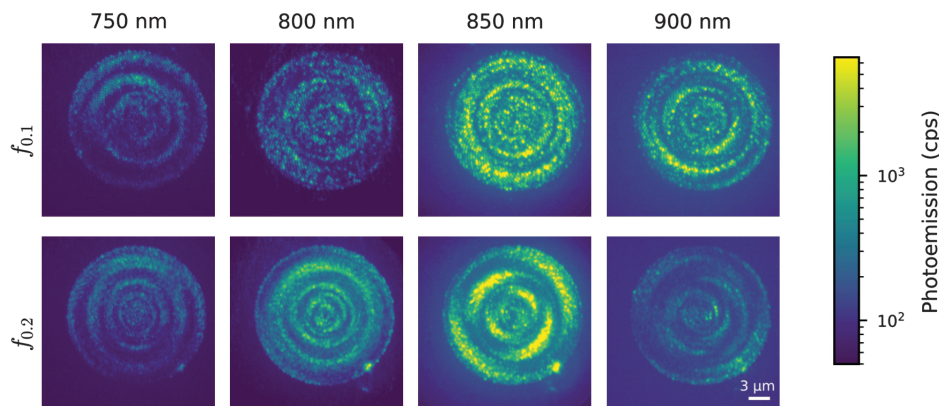


Fig. 3. Electron emission patterns of the two investigated spirals $f_{0.1}$ (top) and $f_{0.2}$ (bottom) recorded at different excitation wavelengths. Constant laser peak intensity over the tuning range of the 100-fs laser pulses is achieved by active power stabilization. The linearly polarized almost normally incident laser pulses are polarized parallel to the horizontal axis in these images.

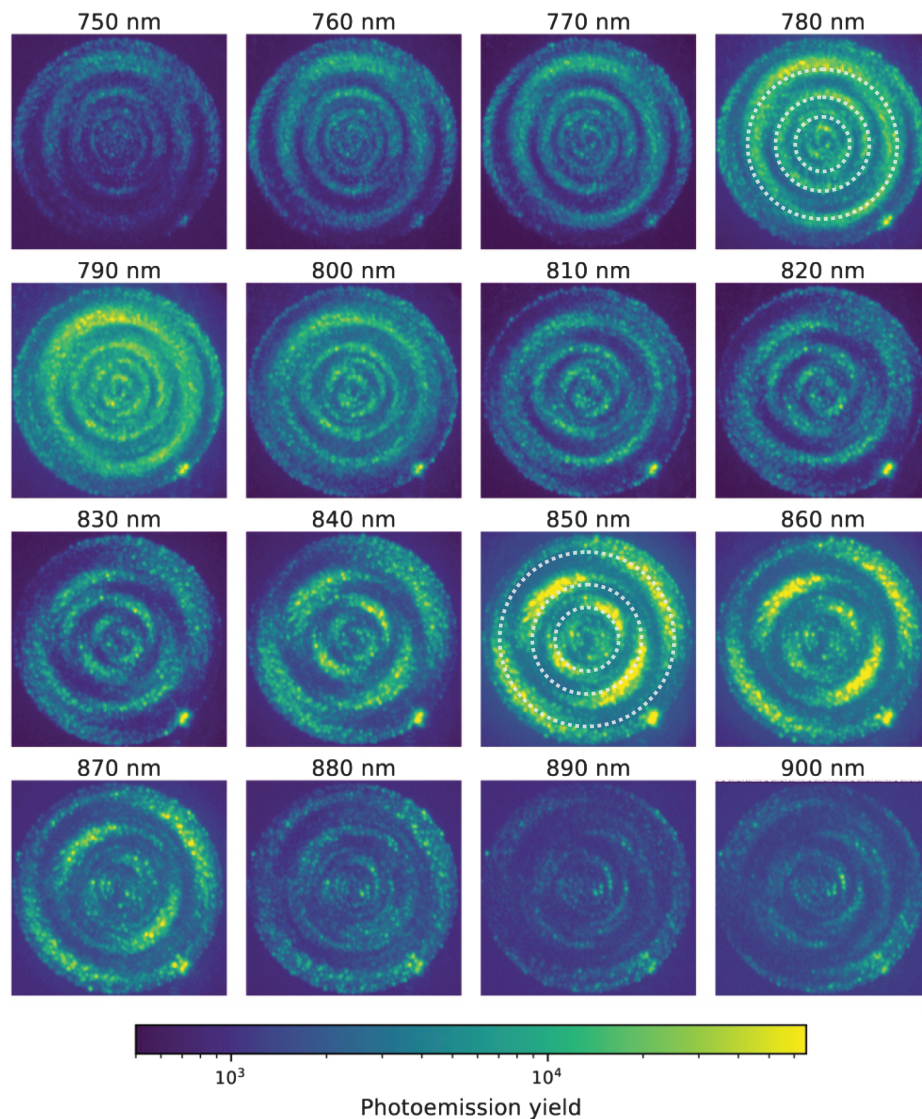


Fig. 4. Wavelength dependence of the total electron emission yield pattern of spiral $f_{0,2}$. To better emphasize the variation of mode patterns, the incident laser pulse energy was not kept constant, but maximum possible average laser power was used for each wavelength instead to increase the total yield. To roughly correct for this variation of the incident light intensity and the corresponding strong variation of the yield, the shown emission yields were scaled assuming a quadratic dependence of the yield with intensity. In the patterns for 780 nm and 850 nm excitation, the ring structure discussed in the text is emphasized by dashed white lines.

diagonals, and for subsequent rings their orientation alternates by 90° . In the intermediate range between 800 and 830 nm, a more complex pattern appears, which seems to consist of a continuous transition between the two former cases. Above 880 nm, the multiple dipolar lobe structure disappears and whirlwind-like segmented spirals appear. Hence, within the tuning range of the excitation wavelength a rather complex emission pattern evolution is obvious, which is further investigated in the following. The significantly different emission patterns have common properties. The yield maxima in the patterns always fall into concentric rings that do not change significantly over the investigated wavelength range. Such concentric rings are clearly visible for the outer three rings indicated in Fig. 4 for 780 nm and 850 nm excitation. Also the emission

pattern within the smallest such ring exhibits a systematic variation. However, for such small lateral dimensions no clear pattern evolution can be extracted from the PEEM images because of the above mentioned granularity of the emission pattern.

Further insight into the observed emission patterns is obtained from the spatial distribution of nearest-neighbor nanohole distances in the Vogel spiral. As already employed in the literature for investigating Vogel spirals [4,6,7,24], a Delaunay triangulation reveals the distance between directly neighboring nanoholes. We used the Python package `scipy.spatial.Delaunay` [25] to break down the point cloud into the smallest possible triangles, from which these nearest-neighbor distances were extracted (Fig. 5). It is apparent that the nearest-neighbor distance distribution in the Vogel spiral also exhibits a concentric ring structure, which directly overlaps with

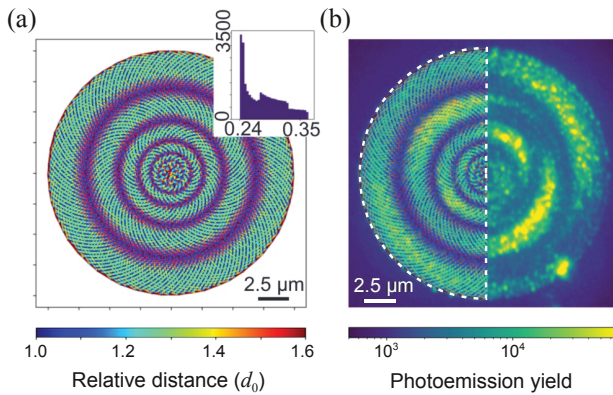


Fig. 5. Comparison between the nearest-neighbor distances within the Vogel spiral $f_{0,2}$ obtained from a Delaunay tessellation and the PEEM emission pattern. (a) Relative distances of nanohole positions plotted as color-coded connection lines between the hole center coordinates. The distances are normalized to the most likely hole separation d_0 in the given spiral structure, which in the present case coincides with the smallest hole separation. The inset shows a histogram of the separations, with the vertical scale showing counts and the horizontal scale showing the distance in micrometers. The jumps in the distribution are commonly observed for golden angle spirals [7,26]. The onset of the distribution is identified as d_0 and used for normalization. (b) Left half circle indicated by the dashed white line: transparent overlay of the nearest-neighbor distance pattern of panel (a) with the PEEM pattern recorded at 850 nm excitation wavelength. Right half of the panel: PEEM pattern exclusively.

the rings from which electron emission is observed. The areas in which strong electron emission is observed always coincide with regions in which the relative distance between neighboring holes is ~ 1.3 , i.e., those regions in which the nanoholes are less densely packed, i.e., where the relative distance between neighboring holes is ~ 1.0 and which appear as blue regions in Fig. 5(a).

To better understand the emission patterns we have performed FDTD simulations for the Vogel $f_{0,2}$ spiral (see Section 3 for details). These simulations yield the electric field inside the a-Si:H waveguide layer that is responsible for electronic excitation. As noted above, in the present case either a multiphoton emission process driven by the local field or thermionic emission can determine the emission yield. In both cases, the electron yield varies nonlinearly with the local excitation in the a-Si:H. For the typical band gap and electron affinity of a-Si:H depending on the actual wavelength at least a three- or four-photon process is needed to emit an electron in a multiphoton emission process. Hence, we model the emission yield as the N th power of the local total field intensity $|\mathbf{E}|^2$, where N is the minimum nonlinear order to overcome the work function for the given wavelength. Note that thermionic emission could also yield similar effective nonlinearities [18].

The resulting emission patterns are shown in Figs. 6(a) and 6(b) for two distinct wavelength values. They show close correspondence to the actually observed patterns at the center wavelength of 780 and 850 nm (compare corresponding panels in Fig. 4). For the shorter wavelength predominant ring-like patterns are observed, and for the longer wavelength dipolar lobes dominate the emission pattern. The similarity between experiment and simulation becomes even more evident if the

full spectral response is considered. The two local field intensity enhancements shown in Fig. 6(c) exhibit two clear resonant peaks, one at about 760 nm and the other at 830 nm, i.e., close to the wavelength values for which the simulated emission patterns are shown [Figs. 6(a) and 6(b)]. Accordingly, the simulation also reveals the resonant character of the experimentally observed emission, which appeared in Fig. 4 as brighter emission patterns. However, the simulated resonances appear at about 20 nm shorter wavelength as compared to the strongest emissions displayed in Fig. 4, which occur for 780 nm and 850 nm. Taking into account that the exact refractive index of the a-Si:H layer is unknown and that an idealized cylindrical hole shape was used for the simulation, a wavelength shift in this order is not unexpected. Note that although the mode pattern looks rather complicated and structured, the local field intensity enhancement exhibits only two distinct resonances, which appear well separated. Since the field intensity enhancement is shown, the width of the resonance in Fig. 6(c) of about 20 nm corresponds to a mode lifetime in the order of about 20 fs assuming a homogeneous linewidth and vanishing pure dephasing. The rather broad resonances in the simulated local spectra are partly due to the fact that the absorption in a-Si:H increases significantly between 900 nm and 700 nm, and partly due to the fact that the modes couple efficiently to the far field. At the present stage of the investigation the contributions of both broadening mechanisms cannot be addressed in more detail.

In theoretical investigations, Dal Negro and coworkers have intensively investigated the mode structure of photonic Vogel spirals [7,26,27]. However, direct experimental evidence for the local fields in Vogel spirals exist to the best of our knowledge only for almost-golden spirals for which localized modes are neither expected nor seen [13]. However, indirect evidence of mode distributions was obtained by photoluminescence (PL) emission microscopy of a spiral structure with embedded color centers [8]. This reveals the spatial variation of the field distribution inside the spiral structure. Lawrence *et al.* used this technique to map field modes that spectrally overlap with the Er related PL emission spectrum and assigned the emission pattern to an incoherent superposition of two localized modes identified with a 2D mode solver [8].

The electron emission patterns reported here have close similarities with photonic band-edge modes [7,26]. We thus discuss the possible identification of these patterns as band-edge modes in the following. Based on theoretically determined local densities of optical states (LDOS) at the center of the spiral, Liew *et al.* identified a photonic band gap covering 0.29 to 0.34 in dimensionless units d_0/λ , where λ is the vacuum wavelength of the light [7]. In this case an ideal 2D structure is assumed; i.e., infinite air cylinders arranged in a golden Vogel spiral pattern are embedded in a homogeneous medium with a refractive index of $n = 2.65$ and infinite thickness. Such ideal 2D structures facilitate calculations since the dimension of the problem is reduced. This treatment does exclude coupling of waveguide modes to the space below and above the spiral structure and disregards one important damping mechanism for photonic modes in real 2D photonic structures. However, the lateral structure used in Ref. [7] is very similar to the structure used in the present investigation. Assuming no impact of either the fill factor, the finite layer thickness, or the different

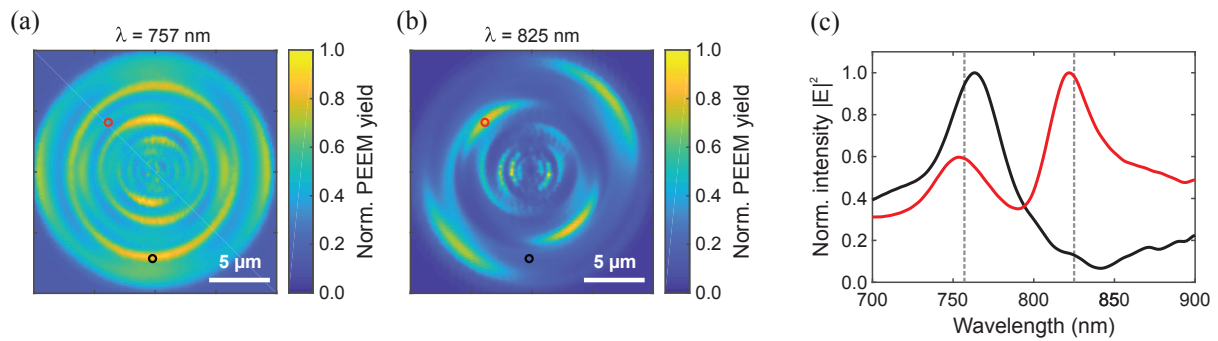


Fig. 6. Electron emission patterns and field response inside the Vogel spiral $f_{0,2}$, with a hole radius of $R = 50$ nm, derived from FDTD simulation for almost normal incidence illumination (incidence angle 4°). (a) and (b) show the electron emission pattern for 757 nm and 825 nm, respectively. The local emission yield is modeled as N th power of the local field intensity ($|E|^2$) distributions inside the a-Si:H material 75 nm below the upper surface. N is the minimum number of absorbed photons required for photoemission fixed to 5 eV, in a multiphoton electron emission process. Therefore, N varies with photon wavelength between 3 and 4 from the short to long wavelength. Fields inside the holes are omitted since these fields do not excite electrons. The emission patterns are laterally averaged using a 2D Gaussian with 300 nm isotropic width (FWHM). Each distribution is normalized to the maximum emission yield. The black and red circles indicate the lateral locations at which the local response shown in (c) was calculated. (c) Local field intensity response, i.e., the ratio between incident field intensity and local field intensity as a function of excitation wavelength. The wavelengths shown in (a) and (b) are indicated as vertical dashed lines.

refractive index of a-Si:H as compared to the literature study [7], the modes that we observed in electron emission (Fig. 4) between 750 and 870 nm cover a range between 0.32 and 0.28 in the same dimensionless units. From this coincidence it seems plausible that the mode pattern observed via PEEM indeed reflects band-edge states. However, neither assuming scaling with the effective refractive index of the layer nor taking the finite layer thickness into account could be questioned, and an unambiguous identification of the mode would require solving Maxwell's equations for the rather large 3D photonic structure with finite thickness and thus coupling to the medium above and underneath the spiral structure. Although we have successfully performed FDTD simulations for the full 3D spiral structure (Fig. 6) we were not yet able to unambiguously identify the band gap. However, as discussed in the following, based on qualitative arguments an identification of the observed modes as class-D band-edge states [7] is at least highly plausible.

Liew *et al.* reported only one class of band-edge states with even azimuthal symmetry, which were labeled as class-D band-edge states [7]. The emission patterns reported here also have even azimuthal symmetry; i.e., either spherical or dipolar lobe patterns are observed. However, the band-edge states reported in Ref. [7] have a significantly smaller normalized size [7]. The nearest-neighbor distribution plot [Fig. 5(a)] can be scaled to match the corresponding radial structure of the nearest-neighbor distribution in Ref. [7]. This scaling reveals that the Vogel spiral used in the present investigation supports four rings in which the distance between neighboring holes is in the range of about $1.3 d_0$ [predominantly the green shaded areas in Fig. 5(a)], whereas the structure in Ref. [7] covers only two such rings. Although the symmetry for the emission patterns reported here and the class-D band-edge states matches, their size relative to the Delaunay tessellation pattern (Fig. 5) differs. This might be explained by the fact that band-edge states in the outer rings are more likely to leak into the surrounding medium. Such states would then appear suppressed and were thus maybe not reported in Ref. [7]. Another explanation for the apparent

discrepancy might be that each ring supports an own set of class-D band-edge states and only the states for the innermost ring are reported in Ref. [7]. The latter argument is supported by the fact that the band-edge states are determined by the arrangement of nanoholes within one ring, as shown in Fig. 10 in Ref. [7]. This means that the mode forms due to light scattering within one ring and the modes are not affected by radially propagating fields coming from other rings.

Since the local nanohole arrangement, i.e., the distance and the direction to the nearest-neighbor nanoholes, in subsequent rings (with relative distances ~ 1.3) has large similarities, the appearance of a class of band-edge states with even azimuthal symmetry in each ring is plausible. The main difference between subsequent rings is the rotational direction of the parastichies, i.e., the spiral arms, which rotate alternately clockwise and counterclockwise. This alternating rotation would also explain the 90° reorientation step for the dipolar lobe emission pattern from ring to ring (best seen in Fig. 4 for 850 nm). This interpretation is consistent with FDTD simulations performed for the 3D spiral structure for rotated spirals. Interestingly, the emission pattern shown in Fig. 6(b) is invariant with this rotation, although the local hole pattern changes. This also indicates that a rotational invariant property must be responsible for the changing orientation of the lobes for the subsequent rings in the Delaunay plot [Fig. 5(b)], and the rotational direction of the parastichies is the main candidate for this invariant property.

On a closer look, the lobes in the dipolar lobe patterns are slightly tilted (see Fig. 4 for 850 nm excitation) with respect to the concentric rings in the Delaunay tessellation. This actually coincides with the shape of the second-order class-D band-edge state [7]. Interestingly, both the experimentally observed (Fig. 4, 850 nm panel) and the simulated emission patterns [Fig. 6(b)] show this tilt of the lobes with respect to the concentric rings. The tilt in the PEEM image and the simulated emission pattern appears to be less pronounced than in the eigenmodes shown in [7]. However, this is attributed to the nonlinear emission

mechanism, which suppresses the weak tails of the lobes and thus renders the tilt less obvious.

The discussion developed above is based primarily on the comparison of the results reported here with the theoretically derived mode structure in ideal 2D spiral structures as described in the literature [7]. As mentioned earlier, in this idealized case, absorption and radiative attenuation are absent for modes propagating outside the 2D plane. Therefore, the modes obtained are well-defined narrow resonances, and a large number of modes appear in the spectral range covered by our wavelength scan. In contrast, our sample exhibits absorption and also considerable radiation damping, and the spectral features are rather broad [Fig. 6(c)] with few clear resonances appearing. Somehow these two extremes must be related, and we anticipate that it will be worthwhile to investigate in future work how the mode structure evolves when one reduces the absorption and decreases the radiative damping by, for example, increasing the thickness of the waveguide.

Based on this qualitative discussion of the substantial similarities between the emission patterns observed by PEEM and the theoretically predicted localized class-D band-edge states in golden spirals, we conclude that the emission pattern reported here indeed reflects the excitation of localized class-D band-edge states in golden Vogel spirals under normal-incidence illumination.

5. CONCLUSION

The results reported here demonstrate that PEEM in combination with a suitable substrate is highly capable of monitoring and investigating electromagnetic modes in photonic structures. In particular, amorphous nanostructured silicon layers combined with FIB milling provide an excellent material platform for further studies of ordered, disordered, and aperiodic photonic structures.

This opens an interesting field for future work since femtosecond laser-assisted PEEM is not limited to just monitoring static modes. Using multipulse excitation sequences, local field dynamics can be resolved [28,29] and local spectroscopic information can be obtained [16,18]. Besides these more methodological aspects, the here-investigated golden Vogel spirals form an interesting photonic playground for investigating localization phenomena of light and orbital angular-momentum photonic modes.

Funding. Deutsche Forschungsgemeinschaft (255652081, 410519108).

Acknowledgment. The principal investigators Martin Aeschlimann, Tobias Brixner, and Walter Pfeiffer acknowledge financial support by the German Research Foundation within the Priority Program “Tailored Disorder - A science- and engineering-based approach to materials design for advanced photonic applications” (SPP 1839). We thank Helmut Stiebig for support with making contact with PVcomB and supervising the substrate fabrication.

Disclosures. The authors declare no conflicts of interest.

Data availability. Data underlying the results presented in this paper are not publicly available at this time but may be obtained from the authors upon reasonable request.

REFERENCES

1. E. Maciá, “Exploiting aperiodic designs in nanophotonic devices,” *Rep. Prog. Phys.* **75**, 036502 (2012).
2. H. Vogel, “A better way to construct the sunflower head,” *Math. Biosci.* **44**, 179–189 (1979).
3. L. Dal Negro and S. V. Boriskina, “Deterministic aperiodic nanostructures for photonics and plasmonics applications,” *Laser Photon. Rev.* **6**, 178–218 (2012).
4. F. Sgrignuoli, R. Wang, F. A. Pinheiro, and L. Dal Negro, “Localization of scattering resonances in aperiodic Vogel spirals,” *Phys. Rev. B* **99**, 104202 (2019).
5. O. J. Trojak, S. Gorsky, C. Murray, F. Sgrignuoli, F. A. Pinheiro, L. Dal Negro, and L. Sapienza, “Cavity-enhanced light–matter interaction in Vogel-spiral devices as a platform for quantum photonics,” *Appl. Phys. Lett.* **118**, 011103 (2021).
6. M. E. Pollard and G. J. Parker, “Low-contrast bandgaps of a planar parabolic spiral lattice,” *Opt. Lett.* **34**, 2805–2807 (2009).
7. S. F. Liew, H. Noh, J. Trevino, L. Dal Negro, and H. Cao, “Localized photonic band edge modes and orbital angular momenta of light in a golden-angle spiral,” *Opt. Express* **19**, 23631–23642 (2011).
8. N. Lawrence, J. Trevino, and L. Dal Negro, “Aperiodic arrays of active nanopillars for radiation engineering,” *J. Appl. Phys.* **111**, 113101 (2012).
9. K. Guo, M. Du, C. I. Osorio, and A. F. Koenderink, “Broadband light scattering and photoluminescence enhancement from plasmonic Vogel’s golden spirals,” *Laser Photon. Rev.* **11**, 1600235 (2017).
10. S. Gorsky, R. Zhang, A. Gok, R. Wang, K. Kebede, A. Lenef, M. Raukas, and L. Dal Negro, “Directional light emission enhancement from LED-phosphor converters using dielectric Vogel spiral arrays,” *APL Photon.* **3**, 126103 (2018).
11. O. J. Trojak, S. Gorsky, F. Sgrignuoli, F. A. Pinheiro, S.-I. Park, J. D. Song, L. Dal Negro, and L. Sapienza, “Cavity quantum electrodynamics with solid-state emitters in aperiodic nano-photonic spiral devices,” *Appl. Phys. Lett.* **117**, 124006 (2020).
12. A. S. Kupriianov, V. R. Tuz, V. I. Shcherbinin, A. Trubin, and V. I. Fesenko, “All-dielectric Vogel metasurface antennas with bidirectional radiation pattern,” *J. Opt.* **22**, 035104 (2020).
13. F. Intonti, N. Caselli, N. Lawrence, J. Trevino, D. S. Wiersma, and L. Dal Negro, “Near-field distribution and propagation of scattering resonances in Vogel spiral arrays of dielectric nanopillars,” *New J. Phys.* **15**, 085023 (2013).
14. M. Bauer, C. Wiemann, J. Lange, D. Bayer, M. Rohmer, and M. Aeschlimann, “Phase propagation of localized surface plasmons probed by time-resolved photoemission electron microscopy,” *Appl. Phys. A* **88**, 473–480 (2007).
15. M. Aeschlimann, M. Bauer, D. Bayer, T. Brixner, S. Cunovic, F. Dimler, A. Fischer, W. Pfeiffer, M. Rohmer, C. Schneider, F. Steeb, C. Strüber, and D. V. Voronine, “Spatiotemporal control of nanooptical excitations,” *Proc. Natl. Acad. Sci. USA* **107**, 5329–5333 (2010).
16. M. Aeschlimann, T. Brixner, A. Fischer, C. Kramer, P. Melchior, W. Pfeiffer, C. Schneider, C. Strüber, P. Tuchscherer, and D. V. Voronine, “Coherent two-dimensional nanoscopy,” *Science* **333**, 1723–1726 (2011).
17. M. Dąbrowski, Y. Dai, and H. Petek, “Ultrafast photoemission electron microscopy: imaging plasmons in space and time,” *Chem. Rev.* **120**, 6247–6287 (2020).
18. M. Aeschlimann, T. Brixner, D. Differt, U. Heinzmann, M. Hensen, C. Kramer, F. Lükermann, P. Melchior, W. Pfeiffer, M. Piecuch, C. Schneider, H. Stiebig, C. Strüber, and P. Thielen, “Perfect absorption in nanotextured thin films via Anderson-localized photon modes,” *Nat. Photonics* **9**, 663–668 (2015).
19. A. V. Shah, H. Schade, M. Vanecek, J. Meier, E. Vallat-Sauvain, N. Wyrsch, U. Kroll, C. Droz, and J. Bailat, “Thin-film silicon solar cell technology,” *Prog. Photovoltaics* **12**, 113–142 (2004).
20. F. Riboli, P. Barthelemy, S. Vignolini, F. Intonti, A. De Rossi, S. Combrie, and D. S. Wiersma, “Anderson localization of near-visible light in two dimensions,” *Opt. Lett.* **36**, 127–129 (2011).
21. K. Vynck, M. Burrese, F. Riboli, and D. S. Wiersma, “Photon management in two-dimensional disordered media,” *Nat. Mater.* **11**, 1017–1022 (2012).

22. D. Pierce and W. Spicer, "Electronic structure of amorphous Si from photoemission and optical studies," *Phys. Rev. B* **5**, 3017–3029 (1972).
23. T. A. F. König, P. A. Ledin, J. Kerszulis, M. A. Mahmoud, M. A. El-Sayed, J. R. Reynolds, and V. V. Tsukruk, "Electrically tunable plasmonic behavior of nanocube–polymer nanomaterials induced by a redox-active electrochromic polymer," *ACS Nano* **8**, 6182–6192 (2014).
24. J. Trevino, H. Cao, and L. Dal Negro, "Circularly symmetric light scattering from nanoplasmonic spirals," *Nano Lett.* **11**, 2008–2016 (2011).
25. "SciPy reference for Delaunay tessellation," <https://docs.scipy.org/doc/scipy/reference/generated/scipy.spatial.Delaunay.html>.
26. J. Trevino, S. F. Liew, H. Noh, H. Cao, and L. Dal Negro, "Geometrical structure, multifractal spectra and localized optical modes of aperiodic Vogel spirals," *Opt. Express* **20**, 3015–3033 (2012).
27. L. Dal Negro, N. Lawrence, and J. Trevino, "Analytical light scattering and orbital angular momentum spectra of arbitrary Vogel spirals," *Opt. Express* **20**, 18209–18223 (2012).
28. P. Kahl, S. Wall, C. Witt, C. Schneider, D. Bayer, A. Fischer, P. Melchior, M. Horn-von Hoegen, M. Aeschlimann, and F.-J. Meyer Zu Heringdorf, "Normal-incidence photoemission electron microscopy (NI-PEEM) for imaging surface plasmon polaritons," *Plasmonics* **9**, 1401–1407 (2014).
29. G. Spektor, D. Kilbane, A. K. Mahro, B. Frank, S. Ristok, L. Gal, P. Kahl, D. Podbiel, S. Mathias, H. Giessen, F.-J. Meyer Zu Heringdorf, M. Orenstein, and M. Aeschlimann, "Revealing the subfemtosecond dynamics of orbital angular momentum in nanoplasmonic vortices," *Science* **355**, 1187–1191 (2017).